Evaluation of multiple SAR speckling filter techniques performance in irrigated rice areas

Andre Dalla Bernardina Garcia[1, 4, 5], Jimuel Jr Celeste[2], Irene Cheng[2, 4], Victor Hugo Rohden Prudente[3], Ieda Del'Arco Sanches[1, 5]

[1] INPE, National Institute for Space Research, PGSER, Remote Sensing Graduate Program, Coordination of Teaching, COEPE, Research and Extension, 12227-010 São José dos Campos, São Paulo, Brazil -(andre.garcia, ieda.sanches)@inpe.br

[2] UoA, University of Alberta, Dept. Of Computing Science, AB T6G 2S4 Edmonton, Alberta, Canada - (jimueljr, iocheng)@ualberta.ca

[3] UofM, University of Michigan, School for Environment and Sustainability, MI 48109 Ann Arbor, United States – victorrp@umich.edu

[4] Multimedia Research Centre, University of Alberta, AB T6G 2E8 Edmonton, Alberta, Canada

[5] DIOTG, Earth Observation and Geoinformatics Division, CG-TG, General Coodination of Earth Science, INPE, National Institute for Space Research, Teaching, COEPE, Research and Extension, 12227-010 São José dos Campos, São Paulo, Brazil

Abstract

Monitoring irrigated rice crops is essential for efficient agricultural management, and Synthetic Aperture Radar (SAR) images are beneficial due to their capability to function in all weather conditions. However, speckle noise in SAR images complicates the classification of land cover. This study evaluates speckle filtering techniques to enhance the image quality of SAR for rice field monitoring. We extend previous work by comparing Bayesian filters in the spatial domain with advanced transform domain methods, including block matching 3D (BM3D) and Discrete Fourier Transform-extracted Edge (DFT Edge) techniques, across different rice growth stages. Twenty-two Sentinel-1B SAR images from the municipality of Turvo, Santa Catarina, Brazil were analyzed. Filters were assessed using metrics for speckle suppression and edge preservation. Our experiments reveal that BM3D with a sigma parameter of 10 ($BM3D_{sigma_{10}}$) provided superior results, balancing effective speckle suppression and edge preservation. Specifically, $BM3D_{sigma_{10}}$ was superior in preserving edge details compared to other techniques. However, as the σ value increased, a loss in resolution was observed, even for the DFT Edge method, which, while efficient in edge preservation, often resulted in reduced detail resolution. These findings highlight the importance of selecting appropriate filtering techniques for accurate agricultural monitoring using SAR data.

1. Introduction

The monitoring of irrigated rice throughout the cultivation period is essential to ensure proper plant development and provide managers with sufficient data to aid in decision-making. The use of remote sensing techniques for this purpose has been increasingly utilized in recent decades, mainly due to the free availability of various satellite images. Among the available images, Synthetic Aperture Radar (SAR) stands out, enabling data acquisition even during periods of high cloud cover, atmospheric moisture, and fine dust particles (Painam and Manikandan, 2021), allowing for cloud-free image generation.

On the other hand, images produced by signals obtained from satellites equipped with SAR sensors exhibit characteristic noise, which is random interference among individual scatters within and around an area of interest pixel, caused by constructive and destructive interference that distorts the radar signal received. This noise, formally Speckle, can introduce variability in classification and cause complications, especially in land cover mappings in agricultural areas (Dingle Robertson et al., 2020). Due to this characteristic, despeckling is a crucial step in the preprocessing of SAR images intended for monitoring and classification of land use and cover. Among the methods for speckle noise filtering, Singh et al. (2021) highlight two approaches: Bayesian approach, which can be categorized into two distinct subclasses, the first operating in the Spatial Domain

and the second in the Transform Domain, and the Non-Bayesian approach.

In our initial study (Garcia et al., 2023), we explored Bayesian filtering techniques in the Spatial Domain, in irrigated rice cultivation areas, and evaluated the impact of these filters on spatial resolution and feature preservation in exchange for speckle noise suppression. However, this initial study focused only on the initial period of irrigated rice development, and the preservation of field boundaries was not evaluated.

In the present study, in addition to reproducing our initial study by adding the evaluation of boundaries and extending the analysis period for the entire crop season, we also added the analysis of filters in the Transform Domain and compared the results with filters in the Spatial Domain, some studies (Singh et al. 2021; Murali et al., 2015) reported that filtering techniques in the Transform Domain generally outperform Spatial Domain approaches. Since edges are important features for land cover segmentation their preservation is a priority. Often, there is a trade-off between smoothness and detail preservation. A filter that balances speckle noise suppression and edge preservation is preferred.

Therefore, the objective of this study is to find a speckle noise filter that effectively removes speckle noise from paddy rice field SAR images while retaining edge details for different stages of rice growth.

2. Material and Methods

2.1 Study Area

Our investigation focuses on the Turvo municipality, situated in the southern region of Santa Catarina (SC), Brazil (Figure 1). This region serves as a primary locus for rice production within this pertinent region recognized for its irrigated rice agriculture in SC. A considerable proportion, namely 50.7%, of the entire area is specifically designated for rice cultivation, representing approximately 12 thousand hectares of land (ANA, 2020).
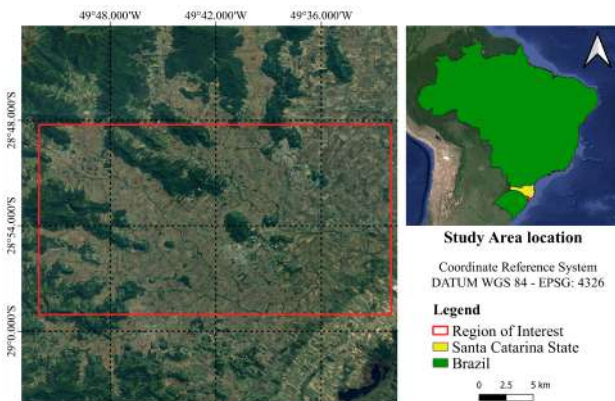

Figure 1. Location of the study area in the state of Santa Catarina, Brazil.

2.2 Satellite data

A total of 22 Sentinel-1B images were downloaded with a 12-day interval between them, using the Google Earth Engine platform. For the download of these images, the 'COPERNICUS/ S1_GRD_FLOAT' collection with linear scale was selected. We opted to use only the images related to VH polarization (vertical emitter - horizontal receiver), because of its sensitivity to the volumetric scattering of rice plants. Among the 22 images, nine were chosen that best represented each month, covering the period from August 2018 to April 2019. This selection aimed to capture various scenes during the development of irrigated rice. Once the images were downloaded and the database was organized, we categorized the images according to their respective periods. For this categorization, we follow the periods and growth cycle schedule of irrigated rice as defined by the Companhia Nacional de Abastecimento (CONAB; National Supply Company) and the Agência Nacional de Águas (ANA; National Water Agency) for the region (ANA, 2020), based on the following schema, with the same number of three months by period:

- Period 1: Beginning of Season (August, 01 - October, 31)

- Period 2: Middle of Season (November, 01 - January, 31)

- Period 3: End of Season (February, 01 - April, 30)

2.3 Speckle filters

Different filters were applied to the representative image to evaluate their performance in reducing speckles, preserving the resolution, and edges of the rice fields. In order to improve our first experiment (Garcia et al., 2023) analysis and results, the same five filters were used in this work. The filters included three adaptive types (Frost, Gamma MAP, and Lee) and two non-adaptive types (Boxcar and Median). Speckle filtering operates by moving a kernel window over each pixel in the image and applying mathematical calculations to replace the value of the central pixel in the window. A 5x5 kernel size was used.

The Boxcar filter performs well in speckle reduction in homogeneous areas but degrades spatial resolution in non-homogeneous areas due to indiscriminate averaging of pixels. The Median filter, while not accounting for speckle properties, effectively removes pulse and spike noise while retaining step and ramp functions (Rana and Suryanarayana, 2019).

The Frost filter, an adaptive and exponentially weighted averaging filter, uses the coefficient of variation, which is the ratio of the local standard deviation to the local mean of the degraded image. The Lee smoothing filter, although adaptive to local statistics, struggles to remove noise in edge regions effectively, but is superior in preserving prominent edges, linear features, point targets, and texture information Santoso et al. (2016). The Gamma filter, a Maximum A Posteriori (MAP) filter based on Bayesian analysis, assumes that both radar reflectivity and speckle noise follow a Gamma distribution, resulting in a K distribution that matches a variety of radar return distributions (Rana and Suryanarayana, 2019).

The transform domain techniques convert an image from the spatial domain to another domain, such as frequency, and then apply noise filtration techniques in that domain. According to a recent comparative study (Singh et al., 2021), transform domain techniques generally surpass spatial domain techniques. These findings inspire the current study to assess transform domain techniques. Specifically, we examine two methods: first, state-of-the-art block-matching 3D transform-domain collaborative filtering (BM3D) (Dabov et al. 2007 and Mäkinen et al. 2020), and second, Boxcar combined with Discrete Fourier Transform-extracted Edge (DFT Edge) (Shitole et al., 2020). The first method, BM3D, is considered state-of-the-art, while the second method, DFT Edge, has shown improvements in edge preservation. This study aims to explore and benefit from the strengths of these methods.

BM3D uses collaborative filtering (Dabov et al. 2007 and Mäkinen et al. 2020). It takes advantage of inherent redundancies in the image, such as similar segments, which explains the collaborative filtering terminology. The method consists of two primary stages: the first is a hard threshold, followed by the Wiener threshold.

The hard threshold is composed of three sub-processes. First, 3D blocks are formed by searching for similar fragments with size $(N_1^{ht})^2$ within the image. The dissimilarity ($l^2-distance$) is applied to Equation (1) to define block-distance (d), of the reference fragment (Z_{x_R}) and another fragment (Z_x), both in the 2D transform domain (T_{2D}^{ht}) applied with a hard threshold (Υ'). Fragments with distances lower than a set threshold (τ_{match}^{ht}) form part of the set of fragments ($S_{x_R}^{ht}$) that are stacked to form a 3D block ($Z_{S_{x_R}^{ht}}$) as Equation (2). With 3D blocks formed, collaborative filtering is performed with a hard threshold (Υ) on the 3D transformation of the 3D block $T_{3D}^{ht}(Z_{S_{x_R}^{ht}})$. Finally, the resulting 3D transformation is transformed back to the spatial domain with an inverse 3D transformation ($T_{3D}^{ht^{-1}}$). The fragments are put back in their original positions and pixels with multiple estimates are aggregated. The resulting image is the basic estimate ($\hat{Y}_{S_{x_R}^{ht}}^{ht}$) as Equation (3).

$$d(Z_{xR}, Z_x) = \frac{||\Upsilon'(T_{2D}^{ht}(Z_{S_{xR}^{ht}})) - \Upsilon'(T_{2D}^{ht}(Z_{S_x^{ht}}))||_2^2}{(N_1^{ht})^2} \quad (1)$$

$$S_{xR}^{ht} = \{x \in X : d(Z_{xR}, Z_x) \leq \tau_{match}^{ht}\} \quad (2)$$

$$\hat{Y}_{S_{xR}^{ht}}^{ht} = T_{3D}^{ht\,-1}(\Upsilon(T_{3D}^{ht}(Z_{S_{xR}^{ht}}))) \quad (3)$$

Wiener threshold utilizes the basic estimate. First, 3D blocks of similar fragments with size $((N_1^{wie})^2)$ are formed from the basic estimate $(\hat{Y}_{xR}^{basic})$ as Equation (4). In this step, the $l^2 - distance$ between fragments are computed in the spatial domain, i.e., $||\hat{Y}_{xR}^{basic}) - \hat{Y}_x^{basic}||_2^2$. With 3D blocks formed from the basic estimate, a second set of 3D blocks are then formed with the original image using the coordinates obtained from the previous step $(Z_{S_{xR}^{wie}})$. Second, the Wiener threshold of the 3D blocks formed from the noisy image is performed in the 3D transform domain $((T_{3D}^{wie}(Z_{S_{xR}^{wie}}))$ using the Wiener Shrinkage Coefficient $(W_{S_{xR}^{wie}})$ as Equations (5) and (6). Note that in its Python implementation Mäkinen et al. (2020) and σ is set as an adjustable parameter. Finally, the resulting 3D transformation is transformed back to the 3D spatial domain with an inverse 3D transformation $(T_{3D}^{wie\,-1})$. The fragments are put back in their original positions and pixels with multiple estimates are aggregated. The resulting image $(\hat{Y}_{S_{xR}^{wie}}^{wie})$ is the final estimate as Equation (6).

$$S_{xR}^{wie} = \{x \in X : \frac{||\hat{Y}_{xR}^{basic} - \hat{Y}_x^{basic}||_2^2}{(N_1^{wie})^2} < \tau_{match}^{wie}\} \quad (4)$$

$$W_{S_{xR}^{wie}} = \frac{||T_{3D}^{wie}(\hat{Y}_{S_{xR}^{wie}}^{basic})||^2}{||T_{3D}^{wie}(\hat{Y}_{S_{xR}^{wie}}^{basic})||^2 + \sigma^2} \quad (5)$$

$$\hat{Y}_{S_{xR}^{wie}}^{wie} = T_{3D}^{wie\,-1}(W_{S_{xR}^{wie}} T_{3D}^{wie}(Z_{S_{xR}^{wie}})) \quad (6)$$

Shitole et al. (2020) proposed a method that utilizes the Discrete Fourier Transform-extracted Edge to improve the edge preservation capacity of a filter. The proposed method first applies a 7x7 Boxcar filter to the noisy image (f) with dimension MxN to remove speckle noise. In a parallel process, the noisy image is transformed with 2D Discrete Fourier Transform as Equation (7). High-pass threshold with rectangular radius (r) is then applied to the 2D transformation (F) to extract the details of the edges. High-frequency components are known to contain edge information of an image (Shitole et al. 2020). The resulting 2D transformation is then transformed back to the spatial domain with Inverse 2D DFT as Equation (8). In this study we call this image as the DFT Edge.

$$F(u, v) = \sum_{x=0}^{M-1} \sum_{y=0}^{N-1} f(x, y) e^{-j2\pi(\frac{ux}{m} + \frac{vy}{N})} \quad (7)$$

The DFT Edge undergoes two additional steps: initially, it is binarized using a threshold, and subsequently, it is despeckled

using a 3x3 Boxcar filter. These steps are executed concurrently. The authors did not specify the rationale for using the 3x3 Boxcar filter, but our hypothesis is that it is employed to eliminate noise originating from the high-pass threshold, as high-frequency components contain speckle noise in addition to edge details.

$$f(x, y) = \frac{1}{MN} \sum_{u=0}^{M-1} \sum_{v=0}^{N-1} f(u, v) e^{j2\pi(\frac{ux}{m} + \frac{vy}{N})} \quad (8)$$

Finally, despeckled DFT Edge is laid on top of the 7x7 Boxcar filtered image with binarized DFT Edge as a reference for replacement. In their analysis, the authors reported that the edge save index of Boxcar improved with DFT Edge with rectangular radius $4 < r < 6$.

2.4 Overall strategy

In the present study four experiments were performed. These experiments cover both spatial domain and transform domain techniques:

- Experiment 1: Spatial filters of our first study (Garcia et al. 2023);

- Experiment 2: BM3D transform domain filter;

- Experiment 3: DFT Edge + Boxcar transform domain filter;

- Experiment 4: Our proposed combination BM3D + DFT Edge;

The BM3D state-of-the-art was optimized using its σ parameter. Five σ configurations were tested, that is, 10, 20, 30, 40, 50. Using this filter parameter is expected to outperform the five spatial domain filters in terms of speckle noise suppression.

The method proposed by Shitole et al. (2020), that is, Boxcar + DFT Edge, was implemented and evaluated, using the radius (r) equal to 3, 4, and 5. In this experiment, the Fast Fourier Transform and the Otsu Thresholding (Xu et al. 2011) were used for 2D Discrete Fourier Transform and DFT binarization, respectively. Python Scipy (Scipy 2D Fast Fourier Transform and Scipy Inverse 2D Fast Fourier Transform) and OpenCV (OpenCV Otsu Thresholding) were utilized in the implementation.

Finally, the results of BM3D for $\sigma = 20$ were combined with DFT Edge, that is, BM3D + DFT Edge, also using the radius (r) equal to 3, 4, and 5. This experiment tests the hypothesis that combining DFT Edge with BM3D state-of-the-art will result in high-quality despeckled images with well-preserved edge details.

In our final analysis, we evaluated three different rice development periods, the beginning, middle and end of the season, in all the mentioned experiments. Consequently, the analyzes resulted in 12 different filter-period combinations.

2.5 Evaluation

Five indices were used to quantify the performance of the filters, namely, Speckle Suppression Index - SSI (Yang et al. 2014), Mean Preservation Index - MPI, Mean Preservation Speckle Suppression Index - MPSSI (Dellepiane and Angiati 2013), Edge Save Index Horizontal - ESIH, and Edge Save Index Vertical - ESIV (Zhang et al. 2009).

The first three indices quantify the speckle suppression capacity of the filters. The last two indices quantify the edge preservation capacity of the filters. For the first three metrics, i.e., SSI, MPI, and MPSSI, a lower value indicates better performance. For the last two indices, that is, ESIH and ESIV, higher values indicate better performance. With M as the original image, F as the filtered image, μ as mean, and σ as standard deviation, the indices are defined as follow Equations (9), (10), (11), (12) and (13):

$$SSI = \frac{S_F}{\mu_F} \cdot \frac{\mu_M}{S_F} \qquad (9)$$

$$MPI = |\frac{\mu_M - \mu_F}{\mu_M}| \qquad (10)$$

$$MPSSI = MPI \cdot |\frac{S_{Fr}}{S_{Mr}}| \qquad (11)$$

$$ESIH = \frac{\sum_{m=1}^{P} \sum_{n=1}^{Q-1} |F_{m,n+1} - F_{m,n}|}{\sum_{m=1}^{P} \sum_{n=1}^{Q-1} |M_{m,n+1} - M_{m,n}|} \qquad (12)$$

$$ESIV = \frac{\sum_{n=1}^{Q-1} \sum_{m=1}^{P} |F_{m+1,n} - F_{m,n}|}{\sum_{n=1}^{Q-1} \sum_{m=1}^{P} |M_{m+1,n} - M_{m,n}|} \qquad (13)$$

To determine the most effective filters, we employed a ranking system that emphasized edge preservation, as described in Equation (14). The values were normalized using the min-max method per metric to create a ranking scale from 0 to 1. This scoring framework was subsequently used to rank the filters.

$$Rank = \frac{(3 - (SSI + MPI + MPSSI)) + (ESIH + ESIV)}{5} \qquad (14)$$

In this evaluation method, greater weights are assigned to ESIH and ESIV, which are considered indicators of edge preservation abilities. A higher score in this context indicates superior edge preservation. The total scores are then divided by 5 to obtain the weighted average.

A qualitative assessment was conducted to assess the model's capability in maintaining the boundaries and edges of rice paddies, compared to other landscape features, along with the uniformity and smoothness of rice features. In addition, we qualitatively examined how well the model retains small elements such as roads and canals located among and within the irrigated rice plots.

3. Experimental results and analysis

Contrary to our expectations, spatial domain filters generally outperformed transform domain filters in our study area and target. Notably, only the $BM3D_{\sigma_{10}}$ filter surpassed the performance of the mean, median, and Lee filters. During the initial stage, $BM3D_{\sigma_{10}}$ demonstrated the lowest values for MPI and MPSSI, second only to $BM3D_{\sigma_{50}}$. Additionally, except for the DFT_{edge} filters, $BM3D_{\sigma_{10}}$ exhibited the highest edge preservation indices, with ESIH and ESIV values of 0.559 and 0.543, respectively. This balance between effective speckle suppression and edge preservation establishes $BM3D_{\sigma_{10}}$ as the superior filter for this stage, as shown in Table 1.

Filter	SSI	MPI	MPSSI	ESIH	ESIV	Rank
Boxcar	0.874	0.001	0.001	0.346	0.337	4
Median	0.829	0.006	0.005	0.345	0.336	5
Lee	0.893	0.00012	0.00011	0.425	0.414	2
Frost	0.890	0.003	0.003	0.422	0.411	3
Gamma MAP	0.930	0.296	0.194	0.462	0.468	16
$BM3D(\sigma_{10})$	0.941	0.00002	0.00002	0.559	0.543	1
$BM3D(\sigma_{20})$	0.889	0.0001	0.0001	0.330	0.309	6
$BM3D(\sigma_{30})$	0.859	0.0002	0.0001	0.246	0.227	7
$BM3D(\sigma_{40})$	0.840	0.0001	0.0001	0.203	0.187	8
$BM3D(\sigma_{50})$	0.827	0.00001	0.00001	0.179	0.165	9
$Box+DFT_{edge_{r4}}$	3.096	0.174	0.476	2.736	2.744	11
$Box + DFT_{edge_{r5}}$	3.128	0.180	0.480	2.769	2.778	15
$Box + DFT_{edge_{r6}}$	3.100	0.181	0.477	2.757	2.761	14
$BM3D + DFT_{edge_{r4}}$	3.091	0.172	0.469	2.728	2.729	10
$BM3D + DFT_{edge_{r5}}$	3.123	0.178	0.474	2.757	2.754	13
$BM3D + DFT_{edge_{r6}}$	3.095	0.179	0.471	2.748	2.746	12

Table 1. Quantitative comparison of normalized speckle filter performance for the beginning stage.

In contrast, the Gamma MAP filter showed the least effectiveness during the initial phase. It provided minimal noise suppression in rice areas, with MPI and MPSSI values of 0.296 and 0.194, respectively, and no edge preservation benefits, as indicated by ESIH and ESIV values of 0.462 and 0.468 (Table 1). Consequently, the filtered image resembled the original one closely. Although DFT_{edge} filters achieved high MPI and MPSSI values, they also had high ESIH and ESIV values, suggesting better edge preservation compared to Gamma MAP, but still inferior to other methods, ranking between the 10th and 15th positions. A significant drawback of DFT methods is their tendency to lose detail and resolution, leading to noise and altered features within rice fields.

For visual inspection, a 'coolwarm' color ramp was applied, where red indicates higher intensity and blue denotes lower intensity of the backscatter signal. As highlighted in Figure 2, blue areas (typically representing flooded soil for pre-germinated rice seeds) exhibited lower VH polarization backs-

catter due to specular reflection, with noticeable noise points in gray and salmon. This noise is partially inherent to SAR images but also includes signals from developing plants or prepared, moist soil. The study area's complexity includes a river, developing crops, soil preparation, and native vegetation.
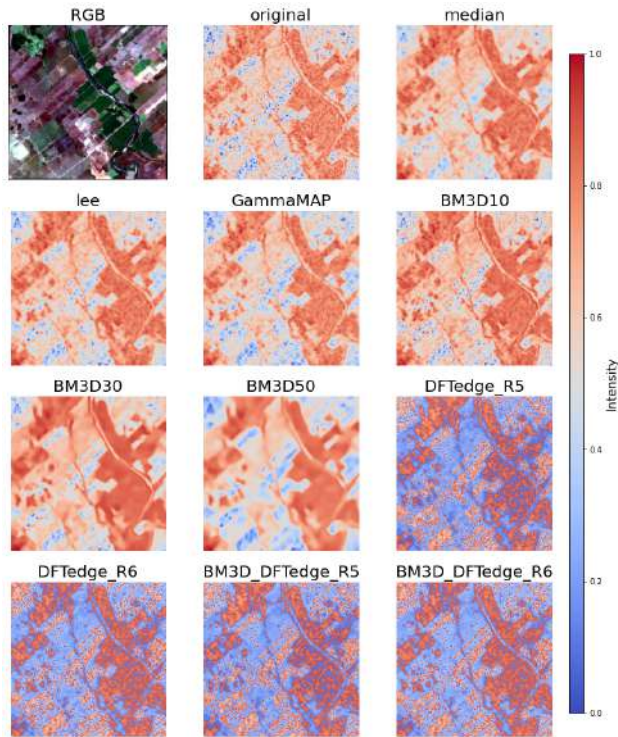

Figure 2. Qualitative analysis of speckle filtering methods for an irrigated rice area at the beginning stage

In summary, blue points and areas indicate low backscatter due to either the absence of vegetation or flooded soil being prepared for rice planting, with fewer structures to alter wave polarization. Conversely, red points signify higher volumetric scattering, associated with dense vegetation. Areas in intermediate colors between salmon and light blue represent stages of vegetation growth or prepared but non-flooded soil, reducing surface smoothness and slightly increasing backscatter response.

At the initial stage, spatial filters performed similarly to $BM3D_{\sigma_{10}}$, with Lee and Median filters effectively smoothing vegetation areas (high intensity/red) and homogenizing medium-intensity areas (salmon color). Gamma MAP's less aggressive smoothing resulted in outcomes similar to the original images, with minimal edge preservation enhancement. Higher sigma values in BM3D filters led to increased smoothing but also resolution loss, with $BM3D_{\sigma_{10}}$ providing the best trade-off between speckle noise suppression and edge preservation. DFT approaches significantly altered some areas, making them overly homogeneous and detail-free, increasing internal noise while improving edge distinction.

In the middle stage, rice cultivation regions appeared homogeneous and predominantly green in RGB channels, with high VH backscatter intensity (Figure 3). Despite visual changes, few ranking alterations occurred, except within the DFT_{edge} filter groups. During this cycle phase, DFT_{edge} filters further altered regions, making it challenging to distinguish rice fields from

other targets, while differentiating dense vegetation from herbaceous or grassy vegetation. As shown in Table 2, $BM3D_{\sigma_{10}}$ continued to perform best, with SSI of 0.880, MPI of 0.00006, MPSSI of 0.00005, ESIH of 0.496, and ESIV of 0.480. Conversely, Gamma MAP again exhibited the least effectiveness, with SSI of 0.891, MPI of 0.295, MPSSI of 0.186, ESIH of 0.439, and ESIV of 0.446.

Filter	SSI	MPI	MPSSI	ESIH	ESIV	Rank
Boxcar	0.805	0.001	0.001	0.308	0.303	4
Median	0.788	0.004	0.003	0.318	0.312	5
Lee	0.823	0.00001	0.00001	0.387	0.380	2
Frost	0.826	0.004	0.003	0.388	0.381	3
Gamma MAP	0.891	0.295	0.186	0.439	0.446	16
$BM3D(\sigma_{10})$	0.880	0.00006	0.00005	0.496	0.480	1
$BM3D(\sigma_{20})$	0.780	0.00014	0.00011	0.241	0.221	6
$BM3D(\sigma_{30})$	0.739	0.00003	0.00002	0.162	0.147	7
$BM3D(\sigma_{40})$	0.719	0.00011	0.00008	0.134	0.121	8
$BM3D(\sigma_{50})$	0.706	0.00025	0.00018	0.119	0.108	9
$Box + DFT_{edge_{r_4}}$	4.971	0.248	0.943	4.345	4.351	13
$Box + DFT_{edge_{r_5}}$	5.091	0.255	0.949	4.482	4.488	12
$Box + DFT_{edge_{r_6}}$	5.100	0.252	0.951	4.554	4.554	10
$BM3D + DFT_{edge_{r_4}}$	4.967	0.247	0.941	4.298	4.296	15
$BM3D + DFT_{edge_{r_5}}$	5.089	0.254	0.945	4.437	4.435	14
$BM3D + DFT_{edge_{r_6}}$	5.098	0.252	0.947	4.505	4.497	11

Table 2. Quantitative comparison of normalized speckle filter performance for the middle stage.

In the final stage, visual inspection revealed distinct regions of high and low signal intensity due to rice harvesting and removal of vegetative and reproductive structures (Figure 4). The original image displayed harvested areas less clearly, with more red and salmon/pink areas. Filtered images from $BM3D_{\sigma_{10}}$, median, and Lee methods more clearly delineated these distinctions, with increased blue regions indicating lower signal intensity. Gamma MAP closely resembled the original image, with minimal noise suppression and no edge preservation enhancement. DFT-filtered images showed aggressive filtering, resulting in small non-noisy areas but introducing high heterogeneity within rice fields, making them unidentifiable. Table 3 indicates that $BM3D_{\sigma_{10}}$ was once more the most proficient filter during this phase, achieving an SSI of 0.842, MPI of 0.00002, MPSSI of 0.00002, ESIH of 0.465, and ESIV of 0.447. In contrast, Gamma MAP was the least effective, with an SSI of 0.887, MPI of 0.295, MPSSI of 0.184, ESIH of 0.439, and ESIV of 0.447.

In analyzing SAR image despeckling techniques, the interaction between radar signals and various elements like vegetation, soil, and water significantly impacts image quality and classification accuracy. The backscatter coefficient of paddy rice fields, which varies with growth stages, is crucial for understanding these interactions. For instance, during the seeding stage, low
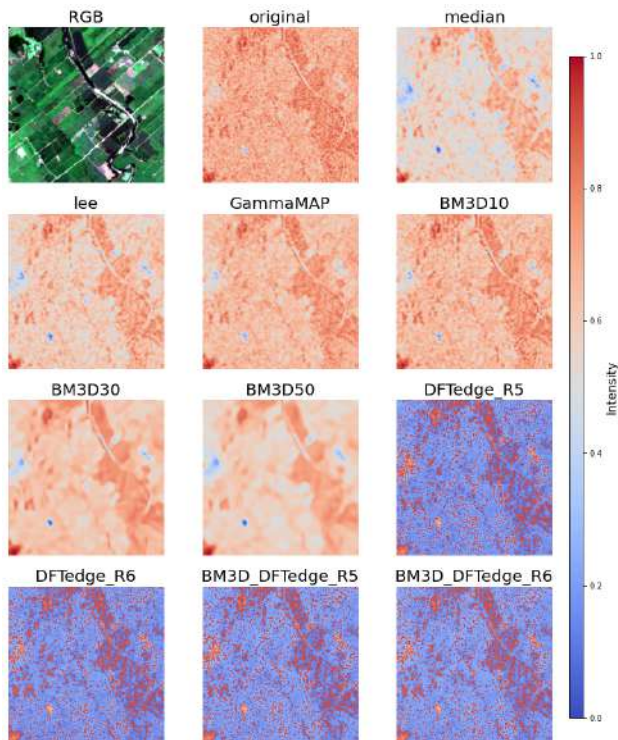
Figure 3. Qualitative analysis of speckle filtering methods for an irrigated rice area at the middle stage
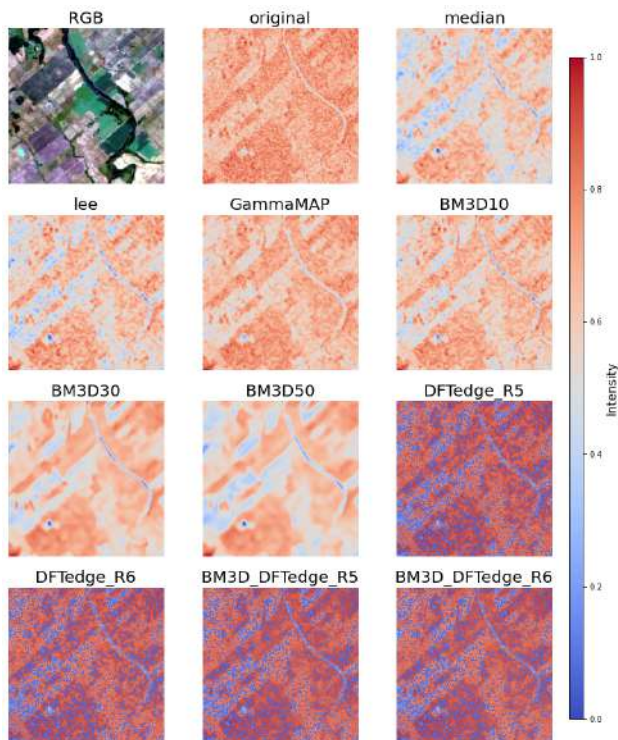
Filter	SSI	MPI	MPSSI	ESIH	ESIV	Rank
Boxcar	0.777	0.001	0.001	0.309	0.303	5
Median	0.752	0.003	0.002	0.320	0.313	4
Lee	0.788	0.000	0.000	0.388	0.379	2
Frost	0.791	0.003	0.003	0.388	0.380	3
Gamma MAP	0.887	0.295	0.184	0.439	0.447	16
$BM3D(\sigma_{10})$	0.842	0.00002	0.00002	0.465	0.447	1
$BM3D(\sigma_{20})$	0.725	0.00006	0.00004	0.214	0.189	6
$BM3D(\sigma_{30})$	0.680	0.00001	0.00001	0.151	0.132	7
$BM3D(\sigma_{40})$	0.656	0.00010	0.00007	0.127	0.112	8
$BM3D(\sigma_{50})$	0.640	0.00023	0.00014	0.114	0.101	9
$Box + DFT_{edge_{r_4}}$	6.533	0.266	1.218	5.255	5.257	12
$Box + DFT_{edge_{r_5}}$	6.439	0.263	1.183	5.175	5.174	10
$Box + DFT_{edge_{r_6}}$	6.473	0.273	1.195	5.207	5.210	13
$BM3D + DFT_{edge_{r_4}}$	6.527	0.265	1.213	5.193	5.185	14
$BM3D + DFT_{edge_{r_5}}$	6.432	0.262	1.178	5.112	5.102	11
$BM3D + DFT_{edge_{r_6}}$	6.466	0.272	1.190	5.145	5.138	15

Table 3. Quantitative comparison of normalized speckle filter performance for the ending stage.

Figure 4. Qualitative analysis of speckle filtering methods for an irrigated rice area at the ending stage

backscatter is observed due to specular reflection from water (Nasirzadehdizaji et al. 2019).

As rice plants grow, backscatter intensity increases due to enhanced interaction with radar waves, peaking at the tillering stage. This observation is evident in our middle-stage analysis, where rice fields displayed high VH backscatter. The $BM3D_{\sigma_{10}}$ filter's high edge preservation indices are crucial for capturing the structural details of growing rice plants. In contrast, the Gamma MAP filter demonstrated lower effectiveness, struggling with both noise suppression and edge preservation. These findings contrast somewhat with Iqbal et al. (2013), which reported superior performance of advanced despeckling techniques, especially those employing selective 3D filtering. In our study, only $BM3D_{\sigma_{10}}$ outperformed traditional methods.

During the harvest phase, our study noted a decrease in VH backscatter and a resurgence in VV polarization, consistent with transitions observed in other studies. This behavior aligns with Chang et al. (2020), which found VH polarization more effective for detecting rice fields. These results underscore the importance of using VH polarization and advanced filters for accurate rice field classification and monitoring.

Speckle noise remains a significant challenge in SAR imagery, affecting image clarity and classification accuracy. Painam and Manikandan (2021) highlights the persistent challenges with speckle reduction techniques, noting that no single method has achieved comprehensive optimization. This issue resonates with our difficulties in identifying small areas and managing classification complexity. The ongoing need for effective speckle reduction methods, as emphasized by Painam and Manikandan (2021), reflects the complexities involved in enhancing SAR image quality.

Singh et al. (2021) discusses how surface roughness and texture affect SAR image brightness and reflectivity, influencing

backscatter signal intensity and classification accuracy. Their findings are relevant to our work, as the texture and roughness of rice fields critically impact backscatter signal variability. Effective filters must accommodate these variations to distinguish different field types accurately and improve overall analysis.

In integrating advanced despeckling methods, our findings do not fully align with the improvements observed by Iqbal et al. (2013) and Murali et al. (2015), where techniques like BM3D and DFT frameworks demonstrated superior performance in preserving image details and reducing speckle compared to traditional methods. In our study, only $BM3D_{\sigma_{10}}$ surpassed the performance of other advanced techniques.

4. Conclusion

Across all growth stages of rice fields, the $BM3D_{\sigma_{10}}$ filter consistently outperforms other methods, effectively balancing speckle suppression with edge preservation. This filter's superior performance is evident across the initial, middle, and final stages of rice growth, demonstrating its robustness in maintaining image clarity and structural details. Conversely, the Gamma MAP filter consistently exhibits the least effectiveness, struggling with both noise reduction and edge preservation. The DFT_{edge} filters, while offering high values for ESIH and ESIV, fall in terms of speckle suppression and often result in excessive loss of detail, placing them in a lower performance tier.

These results highlight the consistent effectiveness of the $BM3D_{\sigma_{10}}$ filter across all growth stages, suggesting that the choice of speckle filter can significantly impact speckle reduction and detail retention regardless of the imaging period. Future work should focus on exploring alternative combinations and enhancements to current filter models. Investigating advanced filter implementations and hybrid approaches may yield improvements in both speckle suppression and edge preservation, leading to better quality SAR images and more accurate classification of rice fields.

Acknowledgements

References

ANA, 2020. Mapeamento do arroz irrigado no Brasil. Agência Nacional de Águas e Saneamento - ANA https://metadados.snirh.gov.br/geonetwork/srv/api/records/1ac9b37f-0745-44f9-a60b-6a2bd366bbe1 (21 August 2020).

Chang, L., Chen, Y.-T., Wang, J.-H., Chang, Y.-L., 2020. Rice-field mapping with Sentinel-1A SAR time-series data. *Remote Sensing*, 13(1), 103. https://doi.org/10.3390/rs13010103.

Dabov, K., Foi, A., Katkovnik, V., Egiazarian, K., 2007. Image denoising by sparse 3-D transform-domain collaborative filtering. *IEEE Transactions on image processing*, 16(8), 2080–2095. https://doi.org/10.1109/TIP.2007.901238.

Dellepiane, S. G., Angiati, E., 2013. Quality assessment of despeckled SAR images. *IEEE Journal of Selected Topics in Applied Earth Observations and Remote Sensing*, 7(2), 691–707. https://doi.org/10.1109/JSTARS.2013.2279501.

Dingle Robertson, L., Davidson, A., McNairn, H., Hosseini, M., Mitchell, S., De Abelleyra, D., Verón, S., Cosh, M. H., 2020. Synthetic Aperture Radar (SAR) image processing for operational space-based agriculture mapping. *International Journal of Remote Sensing*, 41(18), 7112–7144. https://doi.org/10.1080/01431161.2020.1754494.

Garcia, A. D. B., Sanches, I. D., Adami, M., Gama, F. F., 2023. Performance evaluation of speckle filters for paddy rice areas based on sentinel-1 satellite images. *Anais do XX Simpósio Brasileiro de Sensoriamento Remoto*, 20, INPE, Florianópolis, 644–647.

Iqbal, M., Chen, J., Yang, W., Wang, P., Sun, B., 2013. SAR image despeckling by selective 3D filtering of multiple compressive reconstructed images. *Progress In Electromagnetics Research*, 134, 209–226. http://dx.doi.org/10.2528/PIER12091504.

Murali, M. B. Y., Subramanyam, M. V., Prasad, G., 2015. A new approach for SAR image denoising. *International Journal of Electrical and Computer Engineering*, 5(5). http://doi.org/10.11591/ijece.v5i5.pp984-991.

Mäkinen, Y., Azzari, L., Foi, A., 2020. Collaborative filtering of correlated noise: Exact transform-domain variance for improved shrinkage and patch matching. *IEEE Transactions on Image Processing*, 29, 8339–8354. https://doi.org/10.1109/TIP.2020.3014721.

Nasirzadehdizaji, R., Balik Sanli, F., Abdikan, S., Cakir, Z., Sekertekin, A., Ustuner, M., 2019. Sensitivity analysis of multi-temporal Sentinel-1 SAR parameters to crop height and canopy coverage. *Applied Sciences*, 9(4), 655. https://doi.org/10.3390/app9040655.

Painam, R. K., Manikandan, S., 2021. A comprehensive review of SAR image filtering techniques: systematic survey and future directions. *Arabian Journal of Geosciences*, 14(1), 37. https://doi.org/10.1007/s12517-020-06416-1.

Rana, V. K., Suryanarayana, T., 2019. Evaluation of SAR speckle filter technique for inundation mapping. *Remote Sensing Applications: Society and Environment*, 16, 100271. https://doi.org/10.1016/j.rsase.2019.100271.

Santoso, A. W., Bayuaji, L., Sze, L. T., Lateh, H., Zain, J. M., 2016. Comparison of various speckle noise reduction filters on synthetic aperture radar image. *International Journal of Applied Engineering Research*, 11(15), 8760–8767. https://www.ripublication.com/Volume/ijaerv11n15.htm.

Shitole, S., Jain, V., Vanama, V. S. K., 2020. De-speckling of synthetic aperture radar using discrete fourier transform. *IEEE International Geoscience and Remote Sensing Symposium*, IEEE, Waikoloa, HI, USA, 1524–1527.

Singh, P., Diwakar, M., Shankar, A., Shree, R., Kumar, M., 2021. A Review on SAR Image and its Despeckling. *Archives of Computational Methods in Engineering*, 28, 4633–4653. https://doi.org/10.1007/s11831-021-09548-z.

Xu, X., Xu, S., Jin, L., Song, E., 2011. Characteristic analysis of Otsu threshold and its applications. *Pattern recognition letters*, 32(7), 956–961. https://doi.org/10.1016/j.patrec.2011.01.021.

Yang, X., Wu, K., Tang, Y., 2014. A new metric for measuring structure-preserving capability of despeckling of SAR images. *ISPRS journal of photogrammetry and remote sensing*, 94, 143–159. https://doi.org/10.1016/j.isprsjprs.2014.05.002.

Zhang, W., Liu, F., Jiao, L., Hou, B., Wang, S., Shang, R., 2009. SAR image despeckling using edge detection and feature clustering in bandelet domain. *IEEE Geoscience and Remote Sensing Letters*, 7(1), 131–135. https://doi.org/10.1109/LGRS.2009.2028588.